A General Method for Electrochemical Simulations. 2. Application to the Simulation of Steady-State Currents at Microdisk Electrodes: Homogeneous and Heterogeneous Kinetics

John A. Alden and Richard G. Compton*

Physical and Theoretical Chemistry Laboratory, Oxford University, South Parks Road, OXFORD OX1 3QZ, U.K.

Received: July 17, 1997; In Final Form: September 2, 1997[⊗]

ILU preconditioned Krylov subspace methods are used with conformal mappings to simulate the steady-state response of microdisk and hemispherical electrodes with the influence of homogeneous and heterogeneous kinetics. For the microdisk electrode, the conformal mapping of Amatore and Fosset (*J. Electroanal. Chem.* **1992**, *328*, 21) is shown to be superior to that of Verbrugge and Baker (*J. Phys. Chem.* **1992**, *96*, 4572), both in its efficiency for simple electron-transfer problems and in terms of the conditioning of the matrix it produces. The efficiency improvement arising from the use of multipoint Taylor series expressions for boundary conditions is investigated and is found to be highly significant for these systems where edge singularities are removed by the conformal mapping. Convergence at high rate constants is also addressed. The simulations were used to generate working curves at microdisk and spherical/hemispherical electrodes for ECE, DISP1, EC_2E, DISP2, and EC′ mechanisms and a working surface for quasi-reversible heterogeneous kinetics. These allow quantitative mechanistic analysis for these mechanisms without the need for any further simulation. A suite of programs is available to perform this analysis via the World Wide Web (http://physchem.ox.ac.uk:8000/wwwda/). Approximate analytical expressions, where available, are compared with simulated results. The approximate 'equivalence' between microdisk and spherical/hemispherical electrodes is assessed in the presence of heterogeneous and homogeneous kinetics. The results show that while there is no formal physical basis for an equivalence relation, an approximation for many common mechanisms can be generated by treating a microdisk electrode of radius r as if it were a spherical electrode of radius $2r/\pi$. Slightly better results are obtained if the rate constant, k, for a coupled homogeneous reaction at the microdisk electrode is treated as a rate constant of $\pi k/4$ at a spherical electrode of radius $\pi r/4$. Caution is advised, however, since the quality of the approximation is mechanism dependent: the error is reasonably uniform across the ECE, EC_2E, and DISP reactions but increases significantly with substrate concentration in the EC′ reaction.

1. Introduction

Measurement of the steady-state current at microdisk electrodes of different radii is one of the easiest and yet most powerful electrochemical methods for quantitative mechanistic investigations. The methods required to simulate a microdisk electrode are very closely related to those required for scanning electrochemical microscopy[1−3]—in this technique the response of a microdisk electrode is modified by the presence of a substrate within the diffusion layer arising from electrolysis.

The steady-state transport-limited current at a microdisk electrode has been shown[4] to be equivalent to that of a hemispherical electrode of radius $r_{hemi} = 2r_{disc}/\pi$ or a spherical electrode of radius $r_{sphere} = r_{disc}/\pi$. This relationship does not hold before steady state is reached, so is not suitable for use with transient methods such as chronoamperometry[5] and cyclic voltammetry.[11] It also breaks down when chemical kinetics are coupled to the electron transfer.[6,7] However, the material balance equations at a hemisphere are functions of one spatial dimension and are, therefore, analytically soluble for several mechanisms.[8] Thus, the response at a hemispherical electrode has been used as an approximation for that at the 'equivalent' disk electrode for systems with homogeneous kinetics.[9,10]

The transient response of the microdisk electrode has been the subject of many studies.[11] These have employed a wide range of analytical,[6,12−15] semianalytical,[16,17] and finite-difference numerical methods[11,18−21] to model a fairly narrow range of predominantly first-order chemical mechanisms (E, CE, EC,

EC′, ECE, DISP1, and EC_2E). The steady-state response has received less attention,[22] particularly with homogeneous kinetics,[6,23,24] probably because until the recent introduction of efficient fully implicit direct steady-state solution methods such as the strongly implicit procedure (SIP)[25] and Multigrid,[26] the commonly used transient simulation methods using fully explicit Hopscotch[22,24] or semiexplicit alternating direction implicit (ADI)[19] algorithms had to be run for a long time to asymptotically approach steady state. It is possible to use relaxation methods such as successive over-relaxation (SOR) and ADI for a steady-state simulation, but these are considerably less efficient than SIP and especially multigrid methods.[27] Recently, Gavaghan[28] used SOR to investigate the accuracy of microdisk simulations in cylindrical polar coordinates and found that convergence was impeded by the singularity at the disk edge arising from the change in boundary conditions between the electrode surface and insulating surroundings.

To improve the efficiency of numerical simulations, Michael et al.[21] developed a conformal mapping in oblate spheroidal coordinates for the concentration distributions of species near the surface of a microdisk electrode. This has been refined to a closed-space mapping which is better for steady-state simulations by both Amatore and Fosset[22] (based on Newman's seminal work[29]) and Verbrugge and Baker.[30] These mappings mimic the concentration contours radiating from the disk surface and remove the edge singularity[28] arising from the discontinuous boundary conditions necessary to describe the disk in cylindrical polar coordinates. Transient numerical simulations conducted

---

A General Method for Electrochemical Simulations

J. Phys. Chem. B, Vol. 101, No. 46, 1997 **9607**

in these transformed spaces have proved to be accurate with relatively course meshes.[22,31]

The authors attempted to use multigrid and SIP to simulate the microdisk steady-state response but found that the systems of equations resulting from the conformal mappings were too badly conditioned to be solved with these methods. Therefore, the more robust sparse-matrix approach is used which is described in part 1,[32] based on preconditioned Krylov subspace (F11) methods available in the NAG FORTRAN library.[33] Apart from its greater tolerance of ill-conditioned linear systems, this method has the advantage of being free from the constraint of a finite-difference stencil, and therefore, it may be applied to any chemical mechanism at a wide range of electrode geometries. In this work, the method is applied in conjunction with Amatore's and Verbrugge's conformal mappings to simulate the steady-state currents at a microdisk electrode with coupled homogeneous and heterogeneous kinetics. The steady-state current at a spherical electrode is also simulated using the F11 solvers and a closed-space mapping proposed by Amatore.[7]

The efficiencies of the two closed-space mappings are compared for a simple transport-limited electrolysis and a system with homogeneous chemistry. The improvement in efficiency gained by expressing the flux at the electrode surface and the Neumann (no-flux) boundary conditions as n-point Taylor expansions is investigated.

Analytical expressions, including those for equivalent spherical electrodes, are assessed against the simulated disk and spherical electrode responses for mechanisms with heterogeneous or homogeneous kinetics. Working curves are generated for a range of common first- and second-order mechanisms which allow quantitative analysis of kinetic data without resorting to hemispherical approximations. The working curve data together with the appropriate interpolation software is available to perform kinetic analysis via the World Wide Web (http://physchem.ox.ac.uk/~rgc/).

2. Theory

The scheme developed in part 1 allows the mass transport and kinetics to be formulated separately and then summed into the appropriate elements of a sparse matrix. We begin by describing the mass transport to conformally mapped disks and spherical electrodes. In all cases, the mapping is a closed-space expression, with the transformed radial parameter Γ spanning the interval 0−1 corresponding to real distances spanning from zero to infinity. In the case of the microdisk electrode, the second transformed coordinate, θ, is an angular coordinate, sweeping between parallel and normal to the disk surface.

2.1. Simulation of Microdisk Electrodes with a Conformal Mapping. For a single electroactive species (A) undergoing electrolysis, written as a reduction, at steady state:

$$A + e \rightarrow B \tag{1}$$

the transport of species A to a microdisk electrode is given by eq 2, where D_A is the diffusion coefficient of species A, z is the coordinate normal to the surface of the disk, and r is the radial coordinate. If this equation can be solved for the

$$\frac{\partial[A]}{\partial t} = D_A \frac{\partial^2[A]}{\partial z^2} + D_A \frac{\partial^2[A]}{\partial r^2} + \frac{D_A}{r}\frac{\partial[A]}{\partial r} = 0 \tag{2}$$

concentration distribution of species A, the current may be calculated from the concentration gradient at the electrode surface, eq 3, where r_{disk} is the electrode radius and F is the Faraday constant. This equation has been solved using a Bessel expansion[34] to give an analytical expression for the transport-

$$I = 2pFD_A \int_0^{r_{disk}} \frac{\partial[A]}{\partial z}\bigg|_{z=0} r\, dr \tag{3}$$

limited current, eq 4, where $[A]_{bulk}$ is the bulk concentration of species A. The conformal mappings of both Amatore and

$$I_d = 4r_{disk}FD_A[A]_{bulk} \tag{4}$$

Verbrugge operate on the dimensionless variables, eq 5.

$$Z = z/r_{disk};\ R = r/r_{disk};\ \tau = \frac{D_A t}{r_{disk}^2} \tag{5}$$

Amatore uses the following change of variables, eq 6, to

$$R = \frac{\sqrt{1-\theta^2}}{\cos(^\pi/_2\Gamma)};\ Z = \theta \tan(^\pi/_2\Gamma) \tag{6}$$

transform the concentration distribution into (Γ,θ) space so that the mass transport equation (2) becomes eq 7. The dimension-

$$\frac{\partial[A]}{\partial \tau} = \frac{1}{[\theta^2 + \tan^2(^\pi/_2\Gamma)]}\left\{\frac{4}{\pi^2}\cos^2(^\pi/_2\Gamma)\frac{\partial^2[A]}{\partial\Gamma^2} + \frac{\partial}{\partial\theta}\left[(1-\theta^2)\frac{\partial[A]}{\partial\theta}\right]\right\} \tag{7}$$

less current is given by eq 8,[35] (where the dimensionless concentration $a = [A]/[A]_{bulk}$), hence the expression for the current becomes eq 9. Verbrugge[30] compressed Michael's[21]

$$\Psi = \int_0^1 \frac{\partial a}{\partial\Gamma}\bigg|_{\Gamma=0} d\theta \tag{8}$$

$$I = 4r_{disk}FD_A \int_0^1 \frac{\partial[A]}{\partial\Gamma}\bigg|_{\Gamma=0} d\theta \tag{9}$$

oblate spheroidal coordinates through a slightly different transformation, into a into (Γ,θ) space, defined as shown in eq 10. Equation 2 may be written in the transformed coordinates

$$R = \cos\theta \cosh\left(\frac{\Gamma}{1-\Gamma}\right) \tag{10}$$

$$Z = \sin\theta \sinh\left(\frac{\Gamma}{1-\Gamma}\right)$$

as eq 11. Here, the dimensionless current is given by eq 12.

$$\frac{\partial[A]}{\partial\tau} = \frac{1}{\sin^2\theta + \sinh^2\frac{\Gamma}{1-\Gamma}}\left\{\frac{\partial^2[A]}{\partial\theta^2}\tan\theta\frac{\partial[A]}{\partial\theta} + (1 - \Gamma)^4\frac{\partial^2[A]}{\partial\Gamma^2} + \left[(1-\Gamma)^2\tanh\frac{\Gamma}{1-\Gamma} - 2(1-\Gamma)^3\right]\frac{\partial[A]}{\partial\Gamma}\right\} \tag{11}$$

$$\Psi = \frac{\pi}{2}\int_0^{\pi/2} \frac{\partial a}{\partial\Gamma}\bigg|_{\Gamma=0} \cos\theta\, d\theta \tag{12}$$

Hence, the current may be evaluated from eq 13. The boundary

$$I = 2pr_{disk}FD_A \int_0^{\pi/2} \frac{\partial[A]}{\partial\Gamma}\bigg|_{\Gamma=0} \cos\theta\, d\theta \tag{13}$$

conditions necessary to describe a transport-limited electrolysis in both sets transformed coordinates are shown in Table 1. Both of the conformal mappings may be represented (at steady state)

TABLE 1: Boundary Conditions Necessary to Describe a Transport-Limited Electrolysis in Transformed Space

region	boundary condition
$\Gamma = 0$, all θ	$[A] = 0$
$\Gamma = 1$, all θ	$[A] = [A]_{bulk}$
$\theta = 0$, all Γ	$\partial[A]/\partial\theta\|_{\theta=0} = 0$
$\theta = 1$, all Γ (Amatore)	$\partial[A]/\partial\theta\|_{\theta=1 \text{ or } \pi/2} = 0$
$\theta = \pi/2$, all Γ (Verbrugge)	

in the general form given in eq 14, where the κ values represent general coefficients. Equation 14 can be cast into a central finite

$$\frac{\partial[A]}{\partial\tau} = \kappa_{scale}\left\{\kappa_{td}\frac{\partial^2[A]}{\partial\theta^2} + \kappa_{ts}\frac{\partial[A]}{\partial\theta} + \kappa_{gd}\frac{\partial^2[A]}{\partial\Gamma^2} + \kappa_{gs}\frac{\partial[A]}{\partial\Gamma}\right\} = 0 \quad (14)$$

difference form to give eq 15,

$$(-\lambda_{td} + \lambda_{ts})a_{j,k-1} + (-\lambda_{gd} + \lambda_{gs})a_{j-1,k} + (2\lambda_{gd} + 2\lambda_{td})a_{j,k} + (-\lambda_{gd} - \lambda_{gs})a_{j+1,k} + (-\lambda_{td} - \lambda_{ts})a_{j,k+1} = 0 \quad (15)$$

where

$$\lambda_{gd} = \frac{\kappa_{scale}\kappa_{gd}}{(\Delta\Gamma)^2}, \lambda_{gs} = \frac{\kappa_{scale}\kappa_{gs}}{2\Delta\Gamma},$$

$$\lambda_{td} = \frac{\kappa_{scale}\kappa_{td}}{(\Delta\theta)^2}, \text{ and } \lambda_{td} = \frac{\kappa_{scale}\kappa_{ts}}{2\Delta\theta} \quad (16)$$

and $a_{j,k}$ represents the (real) concentration at the finite difference node with indices $j = 1...\text{NGY}$ in the Γ coordinate, $k = 1...\text{NGX}$ in the θ coordinate. Equation 16 may be represented using a general set of pentadiagonal matrix elements $a-e$ as eq 17.

$$a_{j,k}a_{j,k-1} + b_{j,k}a_{j-1,k} + c_{j,k}a_{j,k} + d_{j,k}a_{j+1,k} + e_{j,k}a_{j,k+1} = 0 \quad (17)$$

In part 1, equations of this form are solved using the sparse matrix approach. The flux term in the general scheme for heterogeneous kinetics defined in part 1 is expressed in real space as $F_A = D_A/\Delta z$. To incorporate the conformal mappings into the general scheme, this term must be expressed in terms of the flux to the electrode surface in the transformed space. For Amatore's mapping this becomes eq 18, and for Verbrugge's mapping eq 19.

$$F_A = \frac{D_A}{\Delta\Gamma}\frac{2}{\pi\theta r_{disk}} \quad (18)$$

$$F_A = \frac{D_A}{\Delta\Gamma}\frac{\sin\theta}{r_{disk}} \quad (19)$$

In the simulation, the current is evaluated from a summation of concentrations above the electrode surface. Trapezoidal quadrature was used to approximate the integration, eq 20.

$$\int_0^{\theta_{max}}\frac{\partial[A]}{\partial\Gamma}\Big|_{\Gamma=0}\,d\theta \approx \frac{\Delta\theta}{\Delta\Gamma}\left[\frac{1}{2}a_{1,0} + \sum_{k=1}^{NGX}a_{1,k} + \frac{1}{2}a_{1,NGX+1}\right] \quad (20)$$

Substituting for the boundary values using no flux boundary conditions at $\theta = 0$ and $\theta = \theta_{max}$, gives eq 21.

$$\int_0^{\theta_{max}}\frac{\partial[A]}{\partial\Gamma}\Big|_{\Gamma=0}\,d\theta \approx \frac{\Delta\theta}{\Delta\Gamma}\left[\frac{3}{2}a_{1,1} + \sum_{k=2}^{NGX-1}a_{1,k} + \frac{3}{2}a_{1,NGX}\right] \quad (21)$$

2.2. Simulation of Spherical/Hemispherical Electrodes. It is relatively straightforward to change the electrode geometry in the sparse matrix approach by simply replacing the discretized mass transport equations that the kinetics operate on. The mass transport of a species (A) to a spherical electrode is one-dimensional and reaches a steady state, eq 22, where r is the radial coordinate in a set of spherical polar coordinates. This

$$\frac{\partial[A]}{\partial t} = D_A\left[\frac{\partial^2[A]}{\partial r^2} + \frac{2}{r}\frac{\partial[A]}{\partial r}\right] = 0 \quad (22)$$

may be transformed using the closed-space conformal mapping function, eq 23,[7]

$$\Gamma = 1 - \frac{r_{sphere}}{r} \quad (23)$$

to give, eq 24,

$$\frac{\partial[A]}{\partial t} = D_A\gamma^2\frac{\partial^2[A]}{\partial\Gamma^2} = 0 \quad (24)$$

where

$$\gamma = \frac{(1-\Gamma)^2}{r_{sphere}} \quad (25)$$

This may be converted into a finite difference equation (resulting in a tridiagonal coefficient matrix),

$$-\lambda_s a_{j-1} + (1 - 2\lambda_s)a_j - \lambda_s a_{j+1} = 0 \quad (26)$$

where

$$\lambda_s = \frac{D_A(1 - j\Delta\Gamma)^4}{(r_{sphere}\Delta\Gamma)^2} \quad (27)$$

and a_j represents the (real) concentration at the finite difference node with index $j = 1...\text{NGY}$ in the Γ coordinate. $\Delta\Gamma$ is the distance between nodes. $\Gamma = 0$ corresponds to the electrode surface, and the boundary condition here is as for any other electrode geometry. The $\Gamma = 1$ (or $r \rightarrow \infty$) boundary may be represented using a Dirichlet (bulk concentration) boundary condition. The current may be evaluated from eq 28. In this

$$I = 4\pi r_{sphere}FD_A\frac{\partial[A]}{\partial r}\Big|_{r=r_{sphere}} = 4\pi r_{sphere}^2 FD_A\frac{\partial[A]}{\partial\Gamma}\Big|_{\Gamma=0} \quad (28)$$

case there is no integral to approximate.

2.3. Homogeneous and Heterogeneous Kinetics. Here, we describe a range of common mechanisms which we shall simulate together with analytical approximations of the response which have been reported. Analytical expressions for the steady-state current at a microdisk electrode due to a quasi-reversible couple, eq 29, based on the Butler–Volmer equations, eq 30, have been derived by Bessel integrals,[36] the Mellin transformation with the Wiener–Hopf method,[37] and numerical solutions to elliptic integrals.[38] The dimensionless potential,

$$A + e \rightleftharpoons B \quad (29)$$

$$k_f = k_o \exp(-\alpha\Theta)$$

$$k_b = k_o \exp(\beta\Theta) \quad (30)$$

Θ, is given by eq 31, where E^o is the standard potential, α and β are transfer coefficients, and k_o is the standard electrochemical rate constant. Oldham and Zoski[39] compared these methods

$$\Theta = F(E - E^o)/RT \tag{31}$$

and showed that they were essentially the same, giving rise to an approximate expression for the current, eq 32. The dimen-

$$\frac{I(1 + e^{-\Theta})}{I_{tl}} = \frac{\lambda}{\lambda + \dfrac{2\lambda + 12}{\lambda + 3\pi}} \tag{32}$$

sionless parameter, λ, is given by eq 33, where the dimensionless heterogeneous rate constant is defined as shown in eq 34.

$$\lambda = K_{het}(e^{-\alpha\Theta} + e^{\beta\Theta}) \tag{33}$$

$$K_{het} = \frac{k^o r_{disk}}{D} \tag{34}$$

In an earlier publication,[40] Oldham and Zoski compared the microdisk and hemispherical steady-state voltammograms for reversible, irreversible, and quasi-reversible kinetics.

Most homogeneous mechanisms couple the material balance equations of several species so that each species cannot be solved independently. If all species are to be solved simultaneously, the sparsity pattern of the matrix is more complex than that which can be accommodated using a 5-point stencil method. An ECE mechanism, eq 35, is one of the few mechanisms which

$$A + e \rightarrow B \tag{35}$$

$$B \xrightarrow{k} C$$

$$C + e \rightarrow D$$
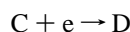
may be solved sequentially if the homogeneous step is irreversible.[25,41] However, as demonstrated in part 1, all species are solved simultaneously in a single sparse matrix in our general mechanism scheme. The steady-state material balance equations for a microdisk electrode are given in eq 36. By rewriting these

$$\frac{\partial[A]}{\partial t} = D_A \frac{\partial^2[A]}{\partial z^2} + D_A \frac{\partial^2[A]}{\partial r^2} + \frac{D_A}{r}\frac{\partial[A]}{\partial r} = 0 \tag{36}$$

$$\frac{\partial[B]}{\partial t} = D_B \frac{\partial^2[B]}{\partial z^2} + D_B \frac{\partial^2[B]}{\partial r^2} + \frac{D_B}{r}\frac{\partial[B]}{\partial r} - k[B] = 0$$

$$\frac{\partial[C]}{\partial t} = D_C \frac{\partial^2[C]}{\partial z^2} + D_C \frac{\partial^2[C]}{\partial r^2} + \frac{D_C}{r}\frac{\partial[C]}{\partial r} + k[B] = 0$$

equations in terms of dimensionless variables, it can be shown that if the diffusion coefficients are assumed equal ($D = D_A = D_B = D_C$), then the ratio of current with kinetics to that of a simple one-electron process (N_{eff}) is a sole function of the dimensionless rate constant (K_{ECE}), eq 37. Alberts and Shain[42]

$$K_{ECE} = \frac{kr_{disk}^2}{D} \tag{37}$$

solved the steady-state material balance equations for a spherical electrode, eq 38. The ECE mechanism has been simulated at

$$N_{eff} = 1 + \frac{\sqrt{2K_{ECE}^{sphere}}}{1 + \sqrt{K_{ECE}^{sphere}}} \quad \text{where } K_{ECE}{}^{sphere} = \frac{kr_{sphere}^2}{D} \tag{38}$$

a microdisk electrode for cyclic voltammetric experiments by Heinze and Störzbach[43] using a time-dependent ADI method.

The steady-state response of a channel microband electrode due to an ECE process has also been simulated using SIP[25] and a multigrid method.[41]

The EC$_2$E mechanism is a second-order analogue of the ECE mechanism, eq 39 in which species may be solved sequentially,[41]

$$A + e \rightarrow B \tag{39}$$

$$2B \xrightarrow{k} C$$

$$C + e \rightarrow D$$
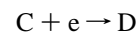
for which the material balance equations are nonlinear, eq 40.

$$\frac{\partial[A]}{\partial t} = D_A \frac{\partial^2[A]}{\partial z^2} + D_A \frac{\partial^2[A]}{\partial r^2} + \frac{D_A}{r}\frac{\partial[A]}{\partial r} = 0 \tag{40}$$

$$\frac{\partial[B]}{\partial t} = D_B \frac{\partial^2[B]}{\partial z^2} + D_B \frac{\partial^2[B]}{\partial r^2} + \frac{D_B}{r}\frac{\partial[B]}{\partial r} - 2k[B]^2 = 0$$

$$\frac{\partial[C]}{\partial t} = D_C \frac{\partial^2[C]}{\partial z^2} + D_C \frac{\partial^2[C]}{\partial r^2} + \frac{D_C}{r}\frac{\partial[C]}{\partial r} + k[B]^2 = 0$$

To be simulated in a fully implicit manner, second-order mechanisms require a nonlinear iterative scheme in addition to a linear solver. As described in part 1, Newton's method may be used with an analytically derived Jacobian which serves as an efficient outer iterative scheme for the nonlinear system inside which the preconditioned Krylov subspace iterative solvers operate.

The steady-state response of a channel microband electrode due to an EC$_2$E process has also been simulated using a multigrid method.[41] As with the ECE mechanism, N_{eff} is a sole function of the dimensionless rate constant (K_{EC2E}) when all species have equal diffusion coefficients, eq 41. However the

$$K_{EC2E} = \frac{k[A]_{bulk}r_{disk}^2}{D} \tag{41}$$

second-order dimensionless rate constant depends on concentration $[A]_{bulk}$.

The DISP mechanisms are limiting cases of the scheme, eq 42. When $k_1 \ll k_2$, the scheme collapses to the first-order DISP1

$$A + e \rightarrow B \tag{42}$$

$$B \xrightarrow{k_1} C$$

$$B + C \xrightarrow{k_2} A + D$$
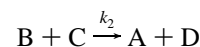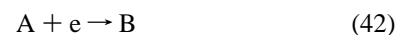
case given in eq 43, which gives rise to another linear set of

$$A + e \rightarrow B \tag{43}$$
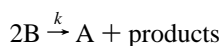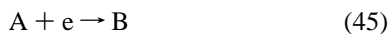
$$2B \xrightarrow{k} A + \text{products}$$

material balance equations, eq 44. If $k_1 \gg k_2$, the second-order

$$\frac{\partial[A]}{\partial t} = D_A \frac{\partial^2[A]}{\partial z^2} + D_A \frac{\partial^2[A]}{\partial r^2} + \frac{D_A}{r}\frac{\partial[A]}{\partial r} + k[B] = 0 \tag{44}$$

$$\frac{\partial[B]}{\partial t} = D_B \frac{\partial^2[B]}{\partial z^2} + D_B \frac{\partial^2[B]}{\partial r^2} + \frac{D_B}{r}\frac{\partial[B]}{\partial r} - 2k[B] = 0$$

DISP2 mechanism results in eq 45, which gives rise to a nonlinear set of material balance equations, eq 45.

$$A + e \rightarrow B \tag{45}$$

$$2B \xrightarrow{k} A + \text{products}$$

$$\frac{\partial [A]}{\partial t} = D_A \frac{\partial^2 [A]}{\partial z^2} + D_A \frac{\partial^2 [A]}{\partial r^2} + \frac{D_A}{r} \frac{\partial [A]}{\partial r} + k[B] = 0 \tag{46}$$

$$\frac{\partial [B]}{\partial t} = D_B \frac{\partial^2 [B]}{\partial z^2} + D_B \frac{\partial^2 [B]}{\partial r^2} + \frac{D_B}{r} \frac{\partial [B]}{\partial r} - 2k[B] = 0$$

As with the ECE and EC$_2$E mechanisms, if the diffusion coefficients of all species are assumed equal, N_{eff} is a sole function of the dimensionless rate constant, eq 47. Unlike the

$$K_{DISP1} = \frac{k r_{disk}^2}{D} \text{ and } K_{DISP2} = \frac{k[A]_{bulk} r_{disk}^2}{D} \tag{47}$$

irreversible ECE and EC$_2$E mechanisms, the material balance equations are bi-directionally coupled so they must be solved simultaneously in a fully implicit simulation. The DISP1 mechanism has been simulated in an explicit time-dependent manner by Ciolkowski[44] using the Hopscotch algorithm. An explicit approximation of the kinetic term might seem attractive, since it decouples the material balance equations allowing each species to be solved sequentially. However, at larger rate constants, ever smaller time steps are necessary to keep the simulation stable, resulting in excessive CPU times.

Fleischmann[10] also derived a corresponding analytical expression for a spherical electrode for the DISP1 mechanism, eq 48.

$$N_{eff} = 2 \frac{1 + \sqrt{2 K_{DISP1}^{sphere}}}{2 + \sqrt{2 K_{DISP1}^{sphere}}} \tag{48}$$

There are no analytical expressions for the steady-state transport-limited current to a spherical electrode for either the EC$_2$E or DISP2 mechanisms to the authors' knowledge.

The EC′ mechanism is closely related to the DISP mechanisms, eq 49, and gives the set of nonlinear simultaneous material balance equations given in eq 50. In this case, N_{eff} is

$$A + e \rightarrow B \tag{49}$$

$$B + C \xrightarrow{k} A + \text{products}$$

$$\frac{\partial [A]}{\partial t} = D_A \frac{\partial^2 [A]}{\partial z^2} + D_A \frac{\partial^2 [A]}{\partial r^2} + \frac{D_A}{r} \frac{\partial [A]}{\partial r} + k[B][C] = 0 \tag{50}$$

$$\frac{\partial [B]}{\partial t} = D_B \frac{\partial^2 [B]}{\partial z^2} + D_B \frac{\partial^2 [B]}{\partial r^2} + \frac{D_B}{r} \frac{\partial [B]}{\partial r} - k[B][C] = 0$$

$$\frac{\partial [C]}{\partial t} = D_C \frac{\partial^2 [C]}{\partial z^2} + D_C \frac{\partial^2 [C]}{\partial r^2} + \frac{D_C}{r} \frac{\partial [C]}{\partial r} - k[B][C] = 0$$

a function of both the dimensionless rate constant ($K_{EC′}$) and the ratio of concentrations (ρ) of substrate to catalyst, eq 51.

$$K_{EC′} = \frac{k[A]_{bulk} r_{disk}^2}{D}; \rho = \frac{[C]_{bulk}}{[A]_{bulk}} \tag{51}$$

Delmastro and Smith[45] solved the mass transport equations at a dropping mercury electrode for the pseudo-first-order case where [C] ≫ [A]. Fleischmann et al.[9] adapted this to give an expression for a spherical electrode, eq 52. Dayton et al.[46] also

$$N_{eff} = 1 + \sqrt{\rho K_{EC′}^{sphere}} \text{ where } K_{EC′}^{sphere} = \frac{k[A]_{bulk} r_{sphere}^2}{D} \tag{52}$$

derived the spherical response using Neumann's integral theorem. Denuault et al.[47,48] derived an analytical expression for the steady state at a spherical electrode due to a second-order EC′ process, where [C] > [A], eq 53. Phillips[6] derived

$$N_{eff} = 1 + \frac{2}{2} [\sqrt{K_{EC′}^{sphere} + 4\rho K_{EC′}^{sphere}} - K_{EC′}^{sphere}] \tag{53}$$

a pair of asymptotic equations for the pseudo-first-order EC′ behavior at a microdisk without resorting to a spherical approximation. The first expression is valid at small rate constants, eq 54. The second expression is valid at large rate

$$N_{eff} = 1 + \frac{2}{\pi} \sqrt{\rho K_{EC′}} + \left(\frac{4}{\pi^2} - \frac{1}{3}\right) \rho K_{EC′} \tag{54}$$

constants, eq 55. The EC′ mechanism has been simulated

$$N_{eff} = \frac{\pi}{4}\left(1 + \sqrt{\rho K_{EC′}} + \frac{1}{4}(\rho K_{EC′})^{-1/2}\right) \tag{55}$$

numerically at a microdisk electrode under pseudo-first-order conditions by Lavagnini et al.[49] using Hopscotch and under second-order conditions by Tutty using ADI.[50]

2.4. Disc/Hemisphere/Sphere 'Equivalence'. As is evident from the previous sections, many analytical approximations for the steady-state transport-limited current to a microdisk electrode are derived by considering an equivalent spherical electrode. It can be seen from Table 2 that are two types of equivalence based on the transport-limited diffusion of a single species at steady-state: (1) Equivalent currents: $r_{disk} = \pi r_{hemi}/2 = \pi r_{sphere}$ and (2) Equivalent average current densities: $r_{disk} = 4 r_{hemi}/\pi = 4 r_{sphere}/\pi$. Since the quantity N_{eff} depends on the ratio of current for a given reaction over that for a simple one-electron process, it may be expressed as either a current or mean current density ratio.

Fleischmann[9,10] and Denuault[47,48] propose that the equivalent current density expression be used to relate systems with homogeneous kinetics. A sphere and hemisphere of the same radius certainly have the same kinetic time scale, with the currents of each species simply scaled by a factor of 2 at the sphere. The approximate relationship between the disk and hemisphere is less intuitive, since the current density is nonuniform at the former but uniform at the latter. Conversely, Amatore[7] suggests the use of a current equivalence relation to relate a microdisk to a hemisphere, stating that while there is no 'formal' equivalence at low rate constants, there is an equivalence in the limit of high rate constants for homogeneous mechanisms. Alden[41] has also used the current equivalence relation to relate a hemispherical cyclic voltammetric response to that of a microdisk including homogeneous EC and EC$_2$ reactions. Ciolkowski et al.[44] use the current equivalence to relate the simulated voltammograms of microdisk and hemispherical electrodes for a DISP1 reaction.

To investigate which of these possible relations is best and how well this approximation holds, let us define a generalized equivalence ratio, ϵ, eq 56. Since the dimensionless first-order

$$r_{sphere} = \epsilon r_{disk} \tag{56}$$

rate constant for a spherical electrode is given by eq 57, we may define an equivalent dimensionless rate constant which should give approximately the same response as the microdisk,

A General Method for Electrochemical Simulations

J. Phys. Chem. B, Vol. 101, No. 46, 1997 **9611**

TABLE 2: Basis for Disc/Sphere/Hemisphere Equivalence

geometry	area	transport-limited current	dimensionless current: $\Psi = I_{lim}/nFDAc$
disc	πr^2	$I_{lim} = 4r_{disk}nFDc$	$\Psi = 4/\pi r_{disk}$
hemisphere	$2\pi r^2$	$I_{lim} = 2\pi r_{hemi}nFDc$	$\Psi = 1/r_{hemi}$
sphere	$4\pi r^2$	$I_{lim} = 4\pi r_{sphere}nFDc$	$\Psi = 1/r_{sphere}$

$$K^{sphere} = \frac{kr_{sphere}^2}{D} \tag{57}$$

eq 58. Alternatively, if the working curve (N_{eff} vs log K^{sphere})

$$K_{rad}^{equiv} = \frac{\epsilon^2 kr_{disk}^2}{D} \tag{58}$$

for a spherical electrode has been calculated/simulated, it may be mapped onto that of the microdisk by replotting N_{eff} against log $K^{sphere} - 2$ log ϵ.

Amatore also suggests[7] for a system with homogeneous kinetics that not only an equivalent radius, but an equivalent rate constant (related by the same ratio) is necessary to map the hemispherical response onto that of the disk. This results in an equivalent dimensionless rate constant, eq 59. Thus, the

$$K_{rad+kin}^{equiv} = \frac{\epsilon^3 kr_{disk}^2}{D} \tag{59}$$

working curve for a spherical electrode should map onto that of the microdisk by replotting N_{eff} against log $K^{sphere} - 3$ log ϵ. Fleischmann and Denuault appear to transform only the electrode radius and not the rate constant for systems with homogeneous kinetics.

Computing

The simulation code was written in C++ calling the NAG FORTRAN library and NAG's beta code for the F11 routines. Callable IDL was also used (via ANSI C wrapper functions) to provide real-time graphics for simulations. The code was compiled (optimized for the mips2 architecture) and executed on a Silicon Graphics Indigo[2] with an R4400 processor and 192 Mb of RAM. To improve the efficiency of the solver when simulating working curves, the solution for the previous rate constant was used as the starting approximation for the next. For typical nonlinear simulations, with steps of 0.2 in log K, this reduced the number of Newton iterations by a factor of 3−6 and the overall number of iterations by a factor of 6−8. The simulation parameters used throughout are shown in Tables 3 and 4.

3. Results and Discussion

We begin by comparing the efficiency of Amatore's conformal mapping with that of Verbrugge for a steady-state transport-limited electrolysis. Both mappings result in concentrations that are invariant in θ, so only Γ convergence needs to be considered. Figure 1 shows the convergence plots in Γ for both the Verbrugge and Amatore conformal mapping, in the form of percent error against the number of nodes in the coordinate of interest (with 100 nodes in the other coordinate).

Increasing the length of the Taylor series from a 2 point approximation significantly improves the convergence in the Γ coordinate. Nevertheless, however the Verbrugge mapping is 'tuned', Amatore's mapping is clearly superior for this mechanism. This is what one would anticipate since the solution to the transport-limited disk steady-state problem in Amatore's space is a plane.[7] Also, the matrix produced by Verbugge's

TABLE 3: Parameters Used in all Simulations

description of parameter	parameter name	value
microdisk radius	r_{disk}	1 μm
initial concentration of reactant	$[A]_{bulk}$	1×10^{-6} mol cm^{-3}
diffusion coefficient (of all species)	D	2×10^{-5} cm^{-2} s^{-1}
solver	METHOD[a]	CGS or BICGSTAB(4)
maximum number of F11 iterations	MAXIT[a]	1000
solver tolerance	TOL[a]	1×10^{-12}
nonlinear tolerance	NLTOL[b]	1×10^{-4}

[a] Parameter names used in the NAG library. [b] Fractional change in current between Newton iterations.

TABLE 4: Optimal Preconditioner Parameters for the Two Conformal Mappings

description of parameter	parameter name	value: Amatore	value: Verbrugge
pivoting strategy	PSTRAT[a]	C (complete)	C (complete)
modified ILU	MILU[a]	N (no)	M (yes)
scaling	EQ[b]	F (no)	T (yes)

[a] Parameter names used in the NAG library. [b] Normalization of each matrix row by the diagonal element to improve conditioning.
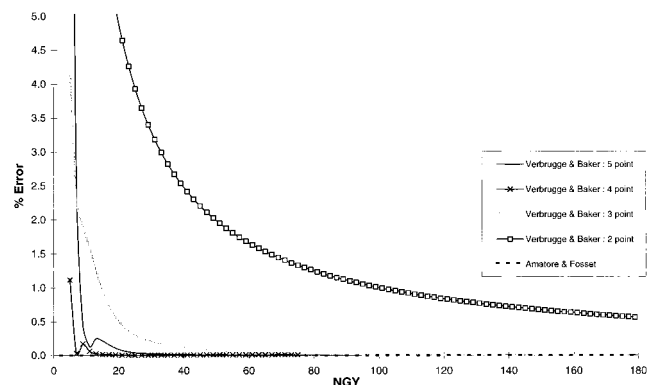

Figure 1. Convergence plot in Γ for a transport-limited electrolysis occurring at a microdisk electrode using an n-point Taylor expression to specify and evaluate the flux to the electrode surface.

transformation is badly conditioned—it has off-diagonally dominant rows and values which span many orders of magnitude.

By examining the transformed mass-transport equation, it is possible to explain the off-diagonal dominance, which presumably resulted in the failed attempts to apply the multigrid solver to this problem. In terms of eq 17, the condition for off-diagonal dominance in this pentadiagonal matrix is given in eq 60. From

$$|a_{j,k}| + |b_{j,k}| + |d_{j,k}| + |e_{j,k}| > |c_{j,k}| \tag{60}$$

eq 15 it can be seen that the conditions for off-diagonal dominance may be separated into components in either coordinate. Either eq 61, which is satisfied when $|\lambda_{ts}| > |\lambda_{td}|$, or eq

$$|\lambda_{td} + \lambda_{ts}| + |\lambda_{td} - \lambda_{ts}| > |2\lambda_{td}| \tag{61}$$

62, which is satisfied when $|\lambda_{gs}| > |\lambda_{gd}|$. Under Verbrugge's

$$|\lambda_{gd} + \lambda_{gs}| + |\lambda_{gd} - \lambda_{gs}| > |2\lambda_{gd}| \tag{62}$$

transformation, the coefficients of the derivatives in the Γ coordinate are as given in eq 63. Hence the inequality $\lambda_{gs} >$

$$\kappa_{gd} = (1 - \Gamma)^4 \text{ and } \kappa_{ts} = (1 - \Gamma)^2\tanh\frac{\Gamma}{1 - \Gamma} - 2(1 - \Gamma)^3 \tag{63}$$

λ_{gd} may be expressed as shown in eq 64. The left-hand-side of

$$\frac{\lambda_{gs}}{\lambda_{gd}} = \frac{\Delta\Gamma\left(\frac{1}{2}\tanh\left(\frac{\Gamma}{1-\Gamma}\right) - (1-\Gamma)\right)}{(1-\Gamma)^2} > 1 \qquad (64)$$

this expression takes its maximum value at NGY when $\Gamma = 1 - \Delta\Gamma$. However, the Dirichlet boundary condition operating at NGY removes one of the two off-diagonal terms, leaving $\lambda_{gd} - \lambda_{gs}$ as the sole off-diagonal contribution, but $2\lambda_{gd}$ remains as the diagonal contribution. Therefore, the condition for diagonal dominance becomes $\lambda_{gs} > 3\lambda_{gd}$, which occurs when

$$\frac{1}{8\Delta\Gamma}\tanh\left(\frac{1-\Delta\Gamma}{\Delta\Gamma}\right) > 1 \qquad (65)$$

Since $\Delta\Gamma = 1/(NGY + 1)$, it can be shown that Verbrugge's mapping gives rise to an off-diagonally dominant matrix if NGY > 7.

It is possible to force the matrix to be diagonally dominant by using downwind differencing to represent the first derivative in the Γ coordinate, hence the finite difference equation becomes that shown in eq 66 and λ_{gs} is redefined as eq 67. This

$$(-\lambda_{td} + \lambda_{ts})a_{j,k-1} + (-\lambda_{gd})a_{j-1,k} + (2\lambda_{gd} + 2\lambda_{td} + \lambda_{gs})a_{j,k} + \\ (-\lambda_{gd} - \lambda_{gs})a_{j+1,k} + (-\lambda_{td} - \lambda_{ts})a_{j,k+1} \quad (66)$$

$$\lambda_{gs} = \frac{\kappa_{scale}\kappa_{gts}}{\Delta\Gamma} \qquad (67)$$

introduces a second-order error term, hence finer meshes would be required in the Γ coordinate to converge the simulation. Even if this measure is taken, the matrix is still badly conditioned due to the large range of values. The resulting precision errors in the (truncated) Gaussian elimination lead to singularities which cause the Gaussian elimination process to fail. Computations were performed with 64 bit double-precision floating point operations, so there was little scope for improvement in the precision of the variables. However, one way to attempt to improve the conditioning is to normalize each row of the matrix (i.e., for a given row, divide each element in **M** and **q** by the diagonal element). This is only effective if the range of values are not too great within a given row. For a simple one-electron process this turns out to be the case—as shown in Table 4, a combination of this scaling procedure and MILU (preserving of row sums in the incomplete Gaussian Elimination process) results in successful ILU preconditioning.

Next, Amatore's space transformation was used to simulate quasi-reversible heterogeneous kinetics. Since the concentration distribution is a plane in Amatore's transformed space for this mechanism, the simulated current is not subject to any convergence error. As the current at the microdisk electrode is a sole function of the dimensionless potential, Θ, and the dimensionless heterogeneous rate constant, the response due to this mechanism may be summarized as a working surface. Figure 2 shows the simulated working surface spanning dimensionless rate constants from 10^{-3} to the Nernstian limit. All the values predicted by eq 32 were within 1% of the simulated values—the maximum error was observed at low rate constants, as the current approached its limiting value.

Next, homogeneous kinetics are addressed, beginning with an ECE mechanism. In contrast to the simple electron transfer, there is no analytical solution to the concentration distribution for either of the conformal mappings. Therefore, one cannot predict a priori whether Amatore's mapping will be better than Verbrugge's. Figures 3 and 4 show convergence plots (in x
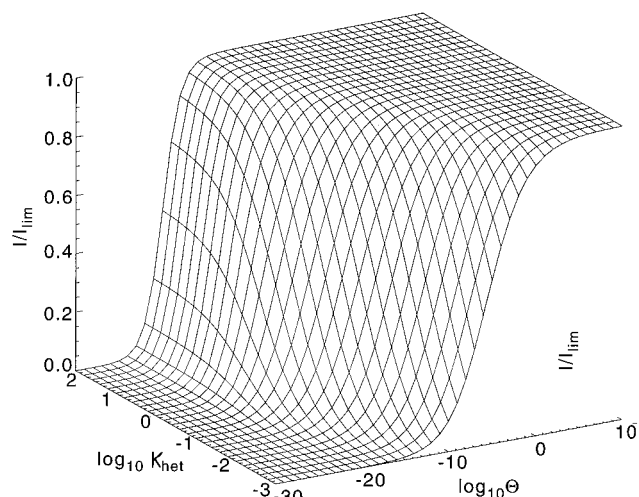

Figure 2. Working surface for a quasi-reversible electron transfer.
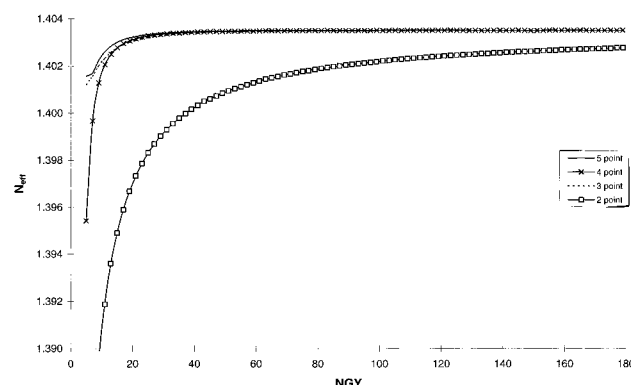

Figure 3. Effect of using an n-point Taylor expression to specify and evaluate the flux to the electrode surface in an ECE simulation.
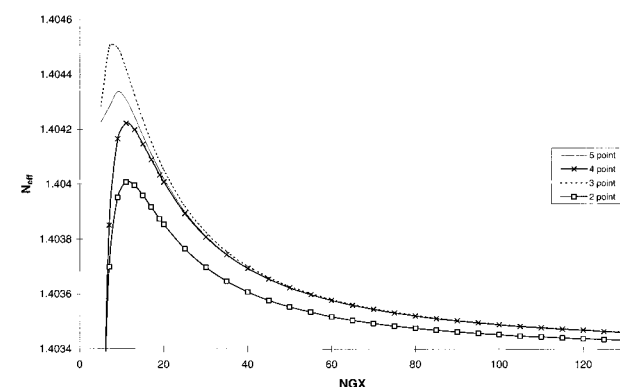

Figure 4. Effect of using an n-point Taylor expression to specify Neumann boundary conditions in an ECE simulation.

and y, respectively) for a simulation of an ECE process with $k = 2000$ s^{-1} for a 1 μm disk using Amatore's coordinate transformation. The linear system arising from application of Verbrugge's conformal mapping to the ECE problem is very badly conditioned. Even after scaling it cannot be solved using either a MILU preconditioned Krylov subspace or a direct Gaussian elimination method for anything larger than a few nodes in either coordinate. It was, therefore, not possible to compare its convergence behavior with Amatore's mapping for systems with homogeneous kinetics.

In addition to providing total mechanistic flexibility, the sparse matrix approach can accommodate an arbitrary n-point Taylor expansion of electrode flux or Neumann boundary conditions. Figure 3 shows the effect on the convergence of an ECE simulation, using 2–5 points in both expressing and
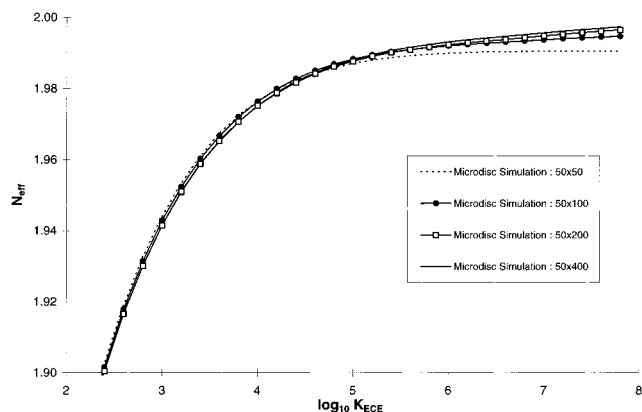
A General Method for Electrochemical Simulations

J. Phys. Chem. B, Vol. 101, No. 46, 1997 **9613**

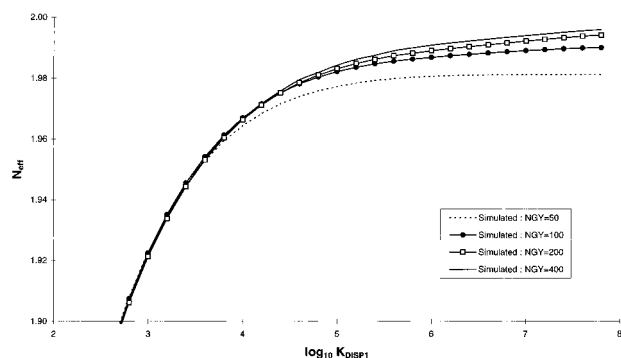**Figure 5.** Convergence of an ECE microdisk simulation at high rate constants.

Figure 6. Convergence of a DISP1 microdisk simulation at high rate constants.

evaluating the flux in the Γ coordinate. The effect on the simulation accuracy is dramatic. This contrasts with Gavaghan's results[28] for a simulation in cylindrical polar space where the disk edge singularity dominates the rate of convergence. As Gavaghan noted, Amatore's and Verbrugge's conformal maps remove this edge singularity and, thus, the limiting factor on convergence becomes the specification/evaluation of the flux at the electrode surface.

Figure 4 shows the effect of simulating an ECE mechanism, using 2−5 point Neumann boundaries in the θ coordinate. Note that in a 5 point stencil method such as SIP (or Multigrid) that a maximum of 3 points may be used to specify the boundaries, though any number may be used to calculate the flux when evaluating the current. A quick examination of the scale of Figure 4 reveals that the simulation is far less sensitive to the number of nodes in the θ coordinate than the Γ coordinate. There is a small discrepancy between the use of a 2 or 3 point Taylor series to express the Neumann boundaries. The effect of increasing the length of the Taylor series further is negligible.

Using an optimal combination of Amatore's mapping, a 4 point flux expression and 3 point Neumann boundary conditions, a simulation with 50×50 nodes gives highly converged results at this rate constant. However, at fast rate constants, the reaction layer (the distance across which species B diffuses away from the electrode) thins and the conformal mapping begins to break down for the species involved in the homogeneous reaction. This is illustrated for an ECE process in Figure 5 and a DISP1 process in Figure 6, showing the convergence breakdown of working curves with large rate constants. For the ECE, EC_2E, DISP1, and DISP2 mechanisms, 400 nodes were necessary in the Γ coordinate to achieve satisfactory convergence (error < 0.2%) over this range. These parameters were used for the simulation of all other homogeneous mechanisms.

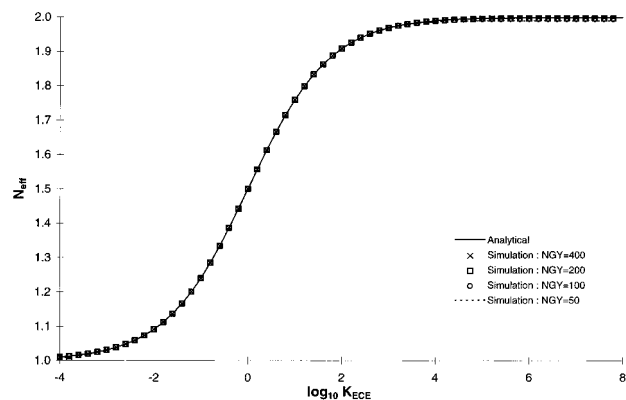The simulated and analytical hemispherical ECE and DISP1

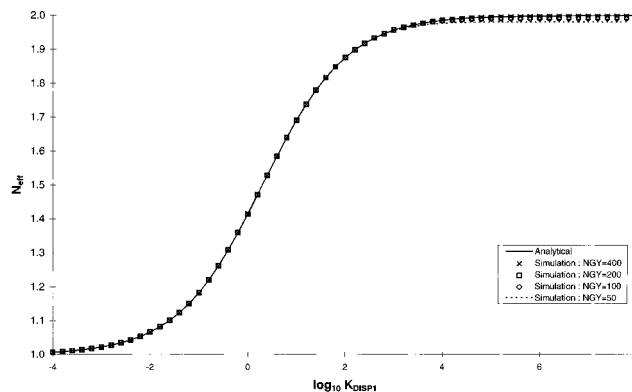**Figure 7.** Simulated and analytical ECE working curves for a hemispherical electrode.

Figure 8. Simulated and analytical DISP1 working curves for a hemispherical electrode.
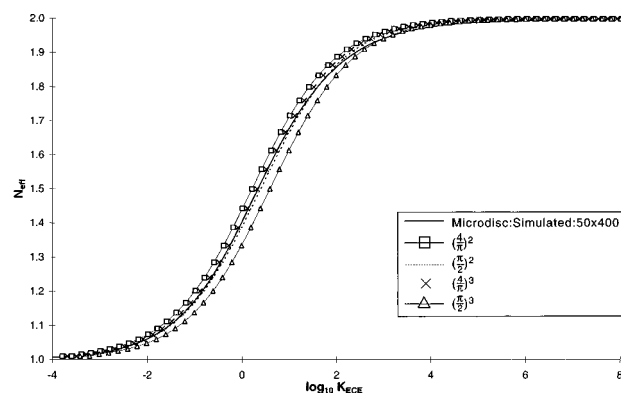

Figure 9. Simulated ECE working curve for the steady-state transport-limited current at a microdisk electrode

working curves are shown in Figures 7 and 8, respectively, providing an indication of the number of nodes necessary to converge the simulations of spherical electrodes at high rate constants. A similar convergence behavior is observed to the closed-space microdisk simulations. For NGY = 400, the simulated and analytical responses are virtually identical. Note the DISP1 process is much more sensitive to the number of nodes in the Γ coordinate. This is because for a given rate constant the concentration distribution of species B spreads out less from the electrode surface for a DISP process than an ECE process.

The full ECE working curve is shown in Figure 9, and the DISP1 working curve is shown in Figure 10. In addition to the simulated microdisk response, the four possible equivalence relations of the spherical response are plotted. The first pair are for an equivalence in terms of radii only: If, as Fleischmann and Denuault suggest, we use a mapping of $\epsilon = \pi/4$ to relate the disk and hemisphere, the responses are significantly shifted.
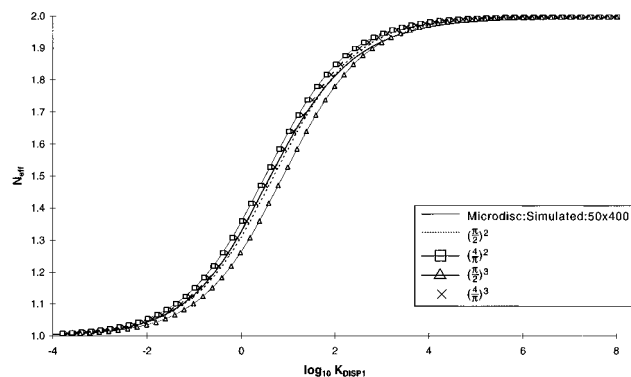
Figure 10. Simulated DISP1 working curve for the steady-state transport-limited current at a microdisk electrode.
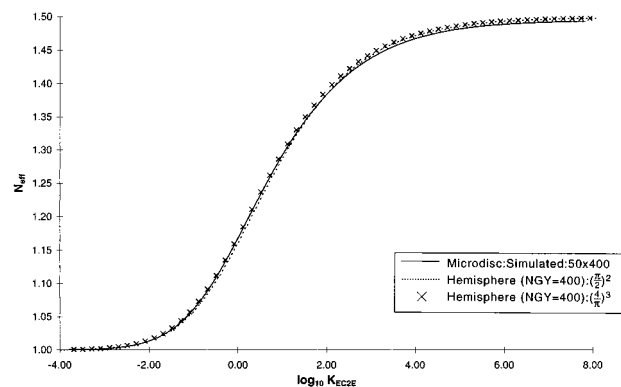

Figure 11. Simulated EC$_2$E working curve for the steady-state transport-limited current at a microdisk electrode.

TABLE 5: Maximum Errors Arising from the Use of Equivalent Spherical Electrodes

	maximum error using sphere with mapping	
mechanism	$2 \log(\pi/2)$	$3 \log(4/\pi)$
ECE	1.2%	0.75%
EC$_2$E	0.63%	0.50%
DISP1	1.4%	1.0%
DISP2	1.3%	0.88%
EC′: $\rho = 0.1$	0.32%	0.39%
EC′: $\rho = 1$	1.06%	1.04%
EC′: $\rho = 10$	7.6%	2.8%
EC′: $\rho = 100$	14.5%	7.7%

If a mapping of $\epsilon = {}^2/_\pi$ is used, however, the curves virtually overlay—fairly close agreement is observed between the microdisk and the spherical responses. The second pair of curves are for an equivalence both in terms of radii and rate constant. The mapping of $\epsilon = {}^\pi/_4$ now produces a result close to the disk response, while the mapping of $\epsilon = {}^2/_\pi$ is not at all close. The fact that $\epsilon = {}^2/_\pi$, applied solely to the radius, and $\epsilon = {}^\pi/_4$, applied to both radius and rate constant, give similar results is not at all surprising since $\log[(\pi/2)^2] = 0.39$ while $\log[(4/\pi)^3] = 0.32$. As is evident from Table 5, the shift of $3 \log(4/\pi)$ produces the better result of the two—the maximum errors are within 1% for both mechanisms.

We now consider second-order homogeneous kinetics. Figure 11 shows the simulated working curve for an EC$_2$E mechanism, and Figure 12 shows that for a DISP2 mechanism. Also shown in these figures are the simulated responses for a hemispherical electrode using the mapping $\epsilon = {}^2/_\pi$ and $\epsilon = {}^\pi/_4$ with ϵ also applied to the rate constant. Again, as shown in Table 5, the latter mapping gives better results with a maximum error of below 1% for both mechanisms.

Figure 13a–d shows the simulated EC′ working curves at a microdisk electrode for ρ values of 0.1, 1, 10, and 100,
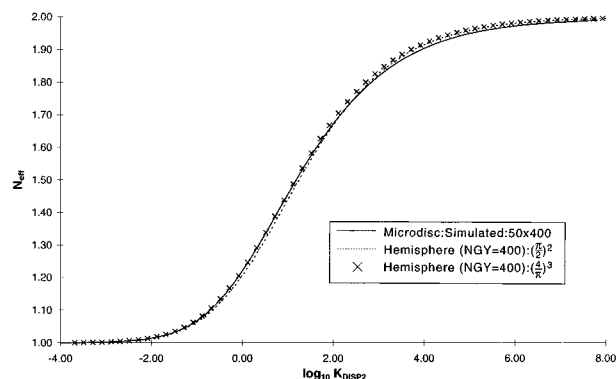

Figure 12. Simulated DISP2 working curve for the steady-state transport-limited current at a microdisk electrode.

respectively. For this mechanism, 50×50 nodes gave highly converged results. In addition, the pseudo-first-order equations (54) and (55) of Phillips are plotted. Also plotted are equations for a spherical electrode (using $\epsilon = {}^\pi/_4$ applied to both the radius and rate constant)—the pseudo-first-order equation of Delmastro and Smith (52) and the second-order equation (53) of Denuault which can be observed to break down at low ρ. For $\rho = 1$, we find (as Denuault did) that the second-order analytical approximation deviates by 2%. For $\rho = 0.1$, the maximum deviation rises to approximately 5%. From the figures and Table 5, the equivalence clearly breaks down with increasing ρ. This means that eq 53 is never a good approximation for the disk. The performance of the pseudo first-order expressions may be evaluated from Figure 14 which corresponds to the pseudo-first-order region of the working curve shown in Figure 13d. Phillips' expressions approximate the disk response quite well, better than the equivalent spherical expression within the pseudo first-order limit, though the asymptotic nature of these expressions is clear. The low K asymptote gives good results for values of $\rho K_{EC'} < 0$, and the large K asymptote gives good results for $\rho K_{EC'} > 0.5$. The two asymptotes break down slightly in the intermediate region, crossing at approximately $\rho K_{EC'} = 0.27$.

4. Conclusions

The sparse matrix scheme developed in part 1, solved using the NAG library F11 (preconditioned Krylov subspace) methods, allows complex mechanisms to be simulated at microelectrodes in a fully implicit manner. The use of a conformal mapping with a 5 point Taylor expansion of the flux allows converged microdisk simulations to be conducted on a grid mesh of 50×50 nodes (50×400 for very high rate constants), resulting in modest CPU times (in the order of tens of seconds).

A working surface has been generated for a quasi-reversible electron transfer at a microdisk electrode, which allows accurate prediction of currents by interpolation across a wide range of rate constants (dimensionless rate constants from 10^{-3} to the Nernstian limit). Working curves have been generated for a range of common homogeneous mechanisms, including EC$_2$E and DISP2 which have not been simulated at this geometry before to the authors' knowledge. Working curves at a hemispherical electrode were also simulated using a closed-space conformal mapping, and similar convergence behavior was found to the Γ coordinate of the microdisk mapping. In all cases, the exact first-order equations agreed with the (converged) simulated hemispherical response. The simulations also allowed spherical responses to be generated for second-order kinetics and the approximate second-order equation of Denuault for the EC′ mechanism to be assessed, which is only valid for high ρ.
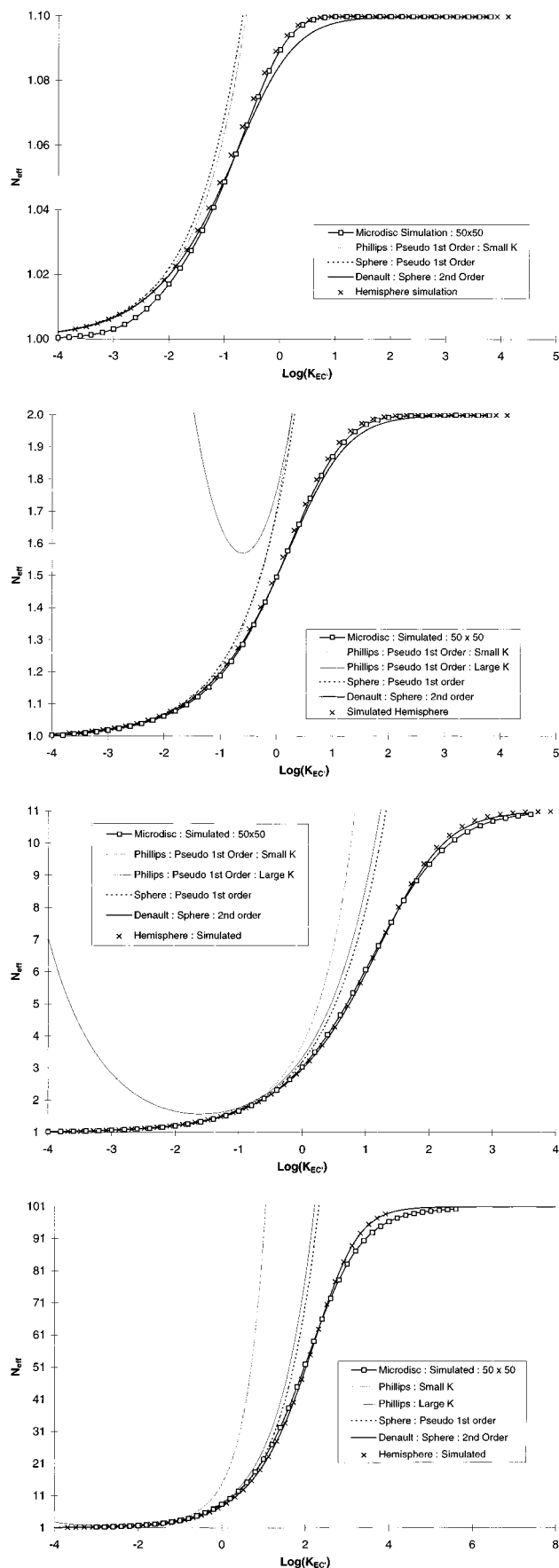
A General Method for Electrochemical Simulations

J. Phys. Chem. B, Vol. 101, No. 46, 1997 **9615**
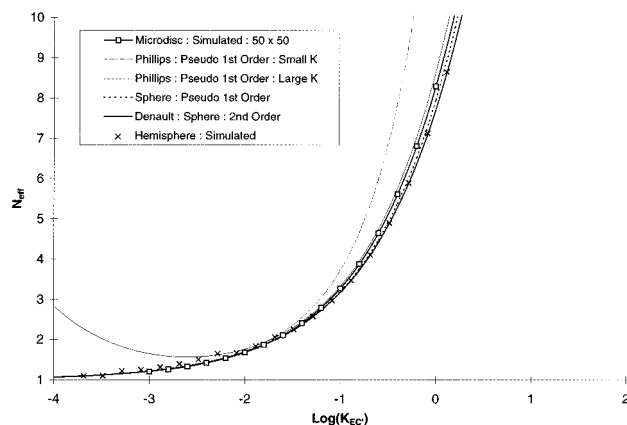
Figure 14. Pseudo first-order region of the simulated EC′ working curve for the steady-state transport-limited current at a microdisk electrode with $\rho = 100$.

ECE, EC$_2$E, DISP1, DISP2, and EC′ reactions. For the former four mechanisms, the pair of approximate equivalence relations $r_{hemi} = \pi r_{disk}/4$ and $k_{hemi} = \pi k_{disk}/4$ (or $K^{equiv} = (\pi^3 k r_{disk}^2)/64D$) may be used to estimate the disk response with a maximum error of 1%. For the EC′ reaction, the equivalence approximation is seen to break down for increasing ρ. This could be attributed to the increasing planarity of the microdisk diffusion layer with increasing ρ and rate constant. For the ECE, EC$_2$E, and DISP mechanisms, the disparity between the disk and equivalent spherical electrode is also greatest at large rate constants (until the limiting behavior at very high rate constants brings the responses together again).

The working curves are available in digital form via the World-Wide-Web (http://physchem.ox.ac.uk:8000) together with programs which allow quantitative analysis for these mechanisms using interpolated values from the working surfaces.

References and Notes

(1) Rubinstein, I. *Physical Electrochemistry*; Bard, A. J., Fan, F.-R., Mirkin, M., Eds.; Marcell-Dekker: New York, 1995; p 209.

(2) Demaille, C.; Unwin, P. R.; Bard, A. J. *J. Phys. Chem.* **1996**, *100*, 14137.

(3) Bard, A. J.; Mirkin, M. V.; Unwin, P. R.; Wipf, D. O. *J. Phys. Chem.* **1991**, *96*, 1861.

(4) Oldham, K. B.; Zoski, C. G. *J. Electroanal. Chem.* **1988**, *256*, 11.

(5) Denuault, G.; Mirkin, M. V.; Bard, A. J. *J. Electroanal. Chem.* **1991**, *308*, 27.

(6) Phillips, C. G. *J. Electroanal. Chem.* **1990**, *296*, 255.

(7) Amatore, C. A.; Fosset, B. *Anal. Chem.* **1996**, *68*, 4377.

(8) Oldham, K. B. *J. Electroanal. Chem.* **1991**, *313*, 3.

(9) Fleischmann, M.; Lasserre, F.; Robinson, J.; Swan, D. *J. Electroanal. Chem.* **1984**, *177*, 97.

(10) Fleischmann, M.; Lasserre, F.; Robinson, J. *J. Electroanal. Chem.* **1984**, *177*, 115.

(11) Alden, J. A.; Hutchinson, F; Compton, R. G. *J. Phys. Chem. B* **1997**, *101*, 949 and references therein.

Figure 13. Simulated EC′ working curves for the steady-state transport-limited current at a microdisk electrode for (a) $\rho = 0.1$, (b) $\rho = 1$, (c) $\rho = 10$, and (d) $\rho = 100$.

The approximate equivalence between microdisk and (hemi)-spherical electrodes has been investigated for homogeneous

(12) Rajendran, L.; Sangaranarayanan, M. V. *J. Electroanal. Chem.* **1996**, *415*, 1.

(13) Aoki, K.; Osteryoung, J. *J. Electroanal. Chem.* **1981**, *122*, 19.

(14) Baker, D. R.; Verbrugge, M. W. *J. Electrochem. Soc.* **1990**, *137*, 3836.

(15) Shoup, D.; Szabo, A. *J. Electroanal. Chem.* **1982**, *140*, 237.

(16) Mirkin, M. V.; Bard, A. J. *J. Electroanal. Chem.* **1992**, *323*, 1.

(17) Jin, B.; Qian, W.; Zhang, Z.; Shi, W. *J. Electroanal. Chem.* **1996**, *420*, 19.

(18) Kakihana, M.; Ikeuchi, H.; Sato, P.; Tokuda, K. *J. Electroanal. Chem.* **1981**, *117*, 201.

(19) Heinze, J. *J. Electroanal. Chem.* **1981**, *124*, 73.

(20) Shoup, D.; Szabo, A. *J. Electroanal. Chem.* **1984**, *160*, 1.

(21) Michael, A. C.; Wightman, R. M.; Amatore, C. A. *J. Electroanal. Chem.* **1989**, *26*, 33.

(22) Amatore, C. A.; Fosset, B. *J. Electroanal. Chem.* **1992**, *328*, 21.

(23) Carofiglio, T.; Magno, F.; Lavagnini, I. *J. Electroanal. Chem.* **1994**, *373*, 1.

(24) Lavagnini, I.; Pastore, P.; Magno, F. *J. Electroanal. Chem.* **1993**, *358*, 193.

(25) Compton, R. G.; Dryfe, R. A. W.; Wellington, R. G.; Hirst, J. *J. Electroanal. Chem.* **1995**, *383*, 13.

(26) Alden, J. A.; Compton, R. G. *J. Electroanal. Chem.* **1996**, *415*, 1.

(27) W. H.; Teukolsky, S. A.; Vetterling, W. T.; Flannery, B. P.; *Numerical Recipes in C: The Art of Scientific Computing*, 2nd ed.; Cambridge University Press: Cambridge, 1992: p 871.

(28) Gavaghan, D. J. *J. Electroanal. Chem.* **1997**, *420*, 147.

(29) Newman, J. *J. Electrochem. Soc.* **1966**, *113*, 501.

(30) Verbrugge, M. W.; Baker, D. R. *J. Phys. Chem.* **1992**, *96*, 4572.

(31) Britz, D. *J. Electroanal. Chem.* **1996**, *406*, 15.

(32) Alden, J. A.; Compton, R. G. *J. Phys. Chem.*, in press.

(33) NAG Fortran Library Mark 18, Section F11, Numerical Algorithms Group, Oxford. The Numerical Algorithms Group has an information desk which may be contacted by email: infodesk@nag.co.uk.

(34) Saito, Y. *Rev. Polarogr.* **1968**, *15*, 177.

(35) We suggest that eq 16 in Amatore's paper[22] should be replaced by eq 8 in this paper.

(36) Bond, A. M.; Oldham, K. B.; Zoski, C. G. *J. Electroanal. Chem.* **1988**, *245*, 71.

(37) Aoki, K.; Tokuda, K.; Matsuda, H. *J. Electroanal. Chem.* **1987**, *235*, 87. Aoki (*Electroanalysis* **1993**, *5*, 627) corrects eq 30 by replacing 4π with $^4/_\pi$.

(38) Baker, D. R.; Verbrugge, M. W. *J. Electrochem. Soc.* **1990**, *137*, 205.

(39) Oldham, K. B.; Zoski, C. G. *J. Electroanal. Chem.* **1991**, *313*, 17.

(40) Oldham, K. B.; Zoski, C. G. *J. Electroanal. Chem.* **1988**, *256*, 11.

(41) Alden, J. A.; Compton, R. G. *J. Phys. Chem.*, in press.

(42) Alberts, G. S.; Shain, I. *Anal. Chem.* **1963**, *35*, 1859.

(43) Heinze, J.; Störzbach, M. *Ber. Bunsen-Ges. Phys. Chem.* **1986**, *90*, 1043.

(44) Ciolkowski, E. L.; Maness, K. M.; Cahill, P. S.; Wightman, R. M.; Evans, D. H.; Fosset, B.; Amatore, C. *Anal. Chem.* **1994**, *66*, 3611.

(45) Delmastro, J. R.; Smith, J. E. *J. Phys. Chem.* **1967**, *71*, 2138.

(46) Dayton, M. A.; Ewing, A. G.; Wightman, R. M. *Anal. Chem.* **1980**, *52*, 2392.

(47) Denuault, G.; Fleischmann, M.; Pletcher, D.; Tutty, O. R. *J. Electroanal. Chem.* **1990**, *280*, 243.

(48) Denuault, G.; Pletcher, D. *J. Electroanal. Chem.* **1991**, *305*, 131.

(49) Lavagnini, I.; Pastore, P.; Magno, F. *J. Electroanal. Chem.* **1993**, *358*, 193.

(50) Tutty, O. R. *J. Electroanal. Chem.* **1994**, *377*, 39.